



Supplement of

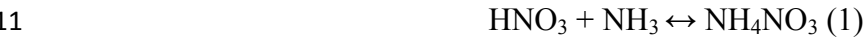
A global model simulation of present and future nitrate aerosols and their direct radiative forcing of climate

D. A. Hauglustaine et al.

Correspondence to: D. A. Hauglustaine (didier.hauglustaine@lsce.ipsl.fr)

8 Model description

9 Free ammonia is used for the neutralization of nitric acid to ammonium nitrate aerosol
10 following the equilibrium reaction:



12 The equilibrium constant (K_p) of (1) strongly depends on relative humidity and temperature.
13 The parameterization used for this dependence is based on Mozurkewich (1993). First, the
14 deliquescence relative humidity (DRH, %) is calculated based on Seinfeld and Pandis (1998):

$$15 \quad \text{DRH} = \exp (723.7/T + 1.6954) \quad (2)$$

16 where T is the air temperature (K). For relative humidities lower than DRH, $K_p = K_{pd}$ and is
17 calculated with:

$$18 \quad K_{pd} = \exp [118.87 - 24084/T - 6.025 \ln(T)] \quad (3)$$

19 For relative humidities higher than DRH, $K_p = K_{ph}$ and depends on both temperature and
20 relative humidity (RH) and is calculated based on :

$$21 \quad K_{ph} = K_{pd} (p_1 - p_2 \text{RH}_1 + p_3 \text{RH}_1^2) \text{RH}_1^{1.75} \quad (4)$$

22 With RH_1 defined as $(1 - \text{RH}/100)$ and p_1 , p_2 , and p_3 provided by:

$$23 \quad p_1 = \exp [-135.94 + 8763/T + 19.12 \ln(T)] \quad (5)$$

$$24 \quad p_2 = \exp [-122.65 + 9969/T + 16.22 \ln(T)] \quad (6)$$

$$25 \quad p_3 = \exp [-182.61 + 13875/T + 24.46 \ln(T)] \quad (7)$$

26

27 Model evaluation

28 Box model simulations

29 In order to evaluate the thermodynamic nitrate aerosol module developed and used in INCA,
30 we have developed a box model version and used it as a stand-alone version to be evaluated
31 against the ISORROPIA version 2.1 reference model (Nenes et al., 1998). Both the INCA box
32 model and ISORROPIA are constrained by the same input parameters. The input parameters
33 are then varied in order to compare the behavior of the two models across the range of

variation in key inputs (i.e., total sulfate TS, total ammonia TA, total nitrate TN, relative humidity RH, and temperature T). The reference input parameters for all simulations are : $T = 280\text{K}$, $RH = 0.9$, $TS = 2 \mu\text{g/m}^3$, $TA = 4 \mu\text{g/m}^3$, and $TN = 5 \mu\text{g/m}^3$. Figure S1 shows the evolution of the simulated NO_3^- and NH_4^+ equilibrium concentrations when these parameters are varied separately over a given interval and compares the output to the ISORROPIA results. Overall an excellent agreement is obtained between the INCA module and ISORROPIA. The sensitivity of the two models to key environmental parameters as encountered in the global atmosphere are very similar and the simulated concentrations in close agreement. The major disagreement we note is at sulfate concentrations larger than about $10 \mu\text{g/m}^3$ for which the INCA module forms ammonium sulfate preferentially and hence significantly underestimates the ammonium nitrate levels compared to ISORROPIA. This disagreement has no effect on the simulated global concentrations since sulfate concentrations larger than $10 \mu\text{g/m}^3$ are hardly reached in the global model grid-cells. It should also be pointed out that at temperature higher than about 295K , the volatilization of ammonium nitrate is too efficient and the concentration simulated with INCA drops more rapidly to zero than in ISORROPIA. This limitation has to be kept in mind but even under a warming climate these high temperatures are not often reached in regions with fine particulate nitrate formation or only occasionally and will have a minor impact on the model results.

Diurnal variations

Nitrate aerosols have the ability to evaporate back into the gas phase. As illustrated by high temporal resolution measurements (e.g., Slanina et al., 2001; Trebs et al., 2004; ten Brink et al., 2007; Dall'Osto et al., 2009; Morgan et al., 2010; Schaap et al., 2011; Mensah et al., 2012; Aan de Brugh et al., 2012), this means that nitrates have a pronounced diurnal cycle and spend most of the daytime in the gas phase. The detailed evaluation of the diurnal cycle is out of the scope of the use of a global model and of this paper. However, since this diurnal variation has an impact on the radiative forcing, we illustrate in Figure S2 the simulated diurnal variation of nitrate concentrations at four different sites for the period 1/8/2009 to 30/10/2009. A very pronounced diurnal cycle is indeed calculated over the Po Valley or over China. As measured at several sites by the studies mentioned above, nitrates build up during the night and reach a maximum concentration early in the morning. The minimum in NO_3^- concentrations occur during daytime due to increased boundary layer height and increased instability at higher temperature, and are often close to zero during that period. This daytime minimum coincides with a maximum in HNO_3 concentrations (not shown) suggesting that

volatilization of nitrate particles indeed occurs as illustrated by several studies (e.g., Dall'Osto et al., 2009; Schaap et al., 2011; Aan de Brugh et al., 2012) . In England, the nitrate concentrations and their variation are in agreement with the range of about 0-12 $\mu\text{g}/\text{m}^3$ and variability measured by Dall'Osto et al. (2009) in October 2006. The variability of NO_3 in the model can be explained by a combination of the diurnal cycle associated with the thermodynamic equilibrium of nitrate formation, superimposed on a variability associated with changing meteorological conditions and transport of pollution episodes from the continent. High pollution episodes of nitrate particles are also simulated in the Netherlands where NH_3 concentrations reach more than 10 $\mu\text{g}/\text{m}^3$.

Present-day nitrate column

Figure S3 shows the three components of the total nitrate column and shows the fine mode, coarse mode on dust and coarse mode on sea-salt separately. This figure clearly shows that fine nitrate particles associated with anthropogenic emissions contribute to a large extent to the maximum calculated in the central US, in Northern Europe and over the Po Valley, in Northern India and in China. Over Africa, Saudi Arabia, Central Europe and in Northern China, nitrates on dust contribute for more than 4-10 mg/m^2 to the nitrate column. Over the Mediterranean and in Southern Europe, the contribution of coarse nitrates on dust represents about 50% of the calculated total nitrate column. The contribution of nitrates on sea-salt is lower and generally close to 0.5 mg/m^2 over the continents. It only reaches 1 mg/m^2 in localized areas, in particular off the coast of the Eastern US, or over the Mediterranean where both pollution and sea-salt particle are present.

Comparison with measurements

Figure S4-S6 compare the simulated and measured surface concentrations of $\text{SO}_4^{=}$, NH_4^{+} , and NO_3^{-} from the EBAS database at NILU. EBAS holds data from EMEP (emep.int), from the US National Atmospheric Deposition Program/National Trend Network (NADP/NTN; <http://nadp.sws.uiuc.edu/NTN>), from the US Inter- agency Monitoring of Protected Visual Environments (IMPROVE; <http://vista.cira.colostate.edu/IMPROVE>), from the Clean Air Status and Trends Network (CASTNET; <http://java.epa.gov/castnet>) and the EANET, Data on the Acid Deposition in the East Asian Region (<http://www.eanet.cc/>). These comparisons have been prepared using the AEROCOM evaluation tools (Schulz et al., 2006). The aerosols measurements are mostly from the CASTNET/IMPROVE network over Northern America,

from the EMEP network in Europe. This evaluation is performed for the year 2006 based on matching daily mean data, averaged to monthly means.

To obtain a large spatial coverage with respect to evaluation of nitrate and ammonium model values we have included measurements from different methods. These use different combinations of filterpacks and denuders. Little harmonization of the methods has been achieved globally and it is not possible to rely on just one method. Depending on filter type, sampling set-up, temperature and changing ambient conditions during a sampling interval considerable sampling artefacts may occur. At higher temperatures, evaporation of ammonium nitrate from filters has been shown to lead to losses of up to 50% in summer conditions (Vecchi et al., 2009; Sickles and Shadwick, 2002; Allegrini et al., 1994; Yu et al., 2005, Hering and Cass, 1999; Chow et al., 2005, Ashbaugh and Elfred, 2004, Schaap et al., 2004, Schaap et al., 2002). Such sampling artefacts may explain in total a positive model bias, while negative model bias clearly points to model errors. We do not find a clear north-south gradient in bias, neither in Europe nor in Northern America, higher temperatures in the south are not associated with higher positive model bias. However, in central Europe there are several sites, where the positive bias of the model is high in summer and almost absent in winter. In depth inspection of nitrate bias on a map and per measurement site may be accessed via the AeroCom web interface (http://aerocom.met.no/cgi-bin/aerocom/surfobs_annualrs.pl?PROJECT=INCA&Run0=LOI_DH10n&Parameter0=SCONC_NO3).

Figure S7-S10 compares the wet deposition of SO_x ($=\text{SO}_2+\text{SO}_4^-$), NH_x ($=\text{NH}_3+\text{NH}_4^+$), and NO_y ($=\text{NO}+\text{NO}_2+\text{NO}_3+\text{HNO}_2+\text{HNO}_3+\text{HNO}_4+2\text{N}_2\text{O}_5+\text{PAN}+\text{organic nitrates}+\text{particulate NO}_3^-$) calculated by the model with the measurements from the EMEP network over Europe, from the NADP network over Northern America and from the EANET network over Eastern Asia. Over the whole dataset, the sulfate deposition is underestimated by the model with a Normalized Mean Bias (NMB) of -59%, mostly driven by a high underestimation over Eastern Asia. Over Europe the deposition is slightly underestimated by the model by 27% and by 20% in Northern America. In Eastern Asia, a higher underestimation of 80% is obtained. The wet deposition of NH_x is underestimated by 34% in the model over the whole dataset. This term is well represented in Europe (NMB=-4.5%) and to a lesser extent in Northern America (NMB=-32%). This deposition term is again significantly underestimated in Eastern Asia (NMB=-60%). The wet deposition of oxidized nitrogen from $\text{HNO}_3+\text{NO}_3^-$ is underestimated by 40% over the whole domain. This deposition term is relatively well

represented in Europe but underestimated by -28% and better represented over Northern America (NMB=+13%). Again, in Eastern Asia, a significant underestimate of the wet deposition is obtained (NMB=-54%).

Figure S11 present an evaluation of the calculated total AOD by comparing with the measurements from the AERONET network (Holben et al., 2001, Kinne et al., 2006). Matching daily data from the model and Aeronet were aggregated to monthly averages. Worldwide, the measured and modeled AOD show a relatively good correlation ($R=0.57$). The arithmetic mean for the measurements of 0.226 is however underestimated by the modeled values of 0.202 with a Normalized Mean Bias (NMB) of -11%. A good agreement with the AERONET measurements is obtained over Northern America. Over this region the model slightly underestimates the measurements (NMB=-4.5%, $R=0.77$). Over Africa, higher AOD associated with dust aerosols are calculated. A fairly good correlation is reached ($R=0.66$) with also a light underestimate by the model of -10%. Over Eastern Asia, the model underestimate the AOD (NMB=-39%). Over Europe, the model slightly overestimates the measurements (NMB=+6%).

Future evolution of atmospheric composition and surface deposition

Figure S12 shows the change in NH_3 surface concentration from the present-day levels in 2030 and 2100 for both RCP4.5 and RCP8.5 (see Fig. 6 from the manuscript for the reference level). For RCP8.5 a significant increase is calculated everywhere in 2030 and 2100 except in Indonesia where biomass burning emissions are reduced. In the central United States, Northern and central Europe, India and China, NH_3 increases by up to $2 \mu\text{g}/\text{m}^3$ in 2100. For the RCP4.5 scenario, a significant increase is still predicted in India and in China where emissions are still predicted to rise. However, concentrations are significantly reduced in Western and Eastern Europe by up to $1 \mu\text{g}/\text{m}^3$ and a lesser increase of $0.5\text{--}1 \mu\text{g}/\text{m}^3$ is calculated in the central US. Figure S13 shows the corresponding change in HNO_3 surface concentrations. Due to a reduction in NO_x emissions, HNO_3 has already significantly decreased in 2030 in Northern America and Europe in both scenarios. In contrast, a strong increase is calculated in India and in China reaching more than $2 \mu\text{g}/\text{m}^3$ in 2030. In 2100, the HNO_3 reduction is almost generalized over the continents with the exception of biomass

burning regions in Africa and India in the case of RCP8.5. Figure S14 shows the change in $\text{SO}_4^{=}$ surface concentration in 2030 and 2100 for both RCP8.5 and RCP4.5. The concentration increases in India and Southeast Asia by more than $2 \mu\text{g}/\text{m}^3$ in 2030. As expected from the sharp decrease in SO_2 emissions, at the end of the XXIst century, a general decrease of the surface concentration is calculated, reaching more than $2 \mu\text{g}/\text{m}^3$ in Northern America, Europe, and China. As a result of these changes in nitrate precursor surface concentrations, nitrate particles are expected to undergo significant variations in the future. Figure S15, shows the evolution of nitrate particles surface concentrations for 2030 and 2100 and for scenarios RCP8.5 and RCP4.5. The surface concentration increases in India and Southeast Asia by more than $2 \mu\text{g}/\text{m}^3$ in 2030. As a consequence of the sharp decrease in HNO_3 concentrations, a decrease of the surface concentration is calculated, reaching more than $2 \mu\text{g}/\text{m}^3$ in Northern America and Europe in 2030 and 2100. This decrease in surface nitrate concentrations also occurs in China in 2100.

Figure S16, shows the change from the present-day (see Fig. 4 from the main paper for reference levels) of the nitrate column in 2030 and 2100 for the two extremes scenarios RCP4.5 and RCP8.5. The change in nitrate precursors is responsible for a strong increase of the nitrate column in the northern hemisphere. The strong decrease in nitrate surface concentrations calculated over Europe and China in 2030 and 2100 dominates the change in the column which decreases by up to $2 \text{ mg}/\text{m}^2$ over these regions.

Figure S17 shows the evolution of the total nitrogen deposition averaged over various regions of the world. The total $\text{NO}_y + \text{NH}_x$ (wet + dry) deposition is presented. In Europe and Northern America, the total N deposition slightly decreases or remains close to its present-day value in the case of scenario RCP8.5. In Asia and India, the NO_y deposition generally increases in 2030 or 2050 due to higher NO_x emissions in these regions before decreasing at the end of the XXIst century. In addition, the NH_x deposition generally increases during the course of the century to reach maximum values in 2100. Figure S18 shows that the fraction of N deposited as NH_x increases from about 60% to 80% in these regions. The same tendency is found over oceanic regions and globally. The total N deposited remains fairly stable or slightly decreases in these regions during the XXIst century but the fraction of N deposited as NH_x increases from 45% to 55-70% over the ocean and from 55% to 70-80% globally.

References

- Aan de Brugh, J. M. J., J. S. Henzing, M. Schaap, W. T. Morgan, C. C. van Heerwaarden, E. P. Weijers, H. Coe, and M. C. Krol, Modelling the partitioning of ammonium nitrate in the convective boundary layer, *Atmos. Chem. Phys.*, 12, 3005-3023, 2012.
- Allegrini, I., A. Febo, C. Perrino and P. Masia, Measurement of Atmospheric Nitric-Acid in Gas-Phase and Nitrate in Particulate Matter by Means of Annular Denuders, *International Journal of Environmental Analytical Chemistry*, 54, 183-201, 1994.
- Ashbaugh, L. L. and R. A. Eldred, Loss of Particle Nitrate from Teflon Sampling Filters: Effects on Measured Gravimetric Mass in California and in the Improve Network, *Journal of the Air & Waste Management Association*, 54, 93-104, 2004.
- Chow, J. C., J. G. Watson, D. H. Lowenthal and K. L. Magliano, Loss of Pm_{2.5} Nitrate from Filter Samples in Central California, *Journal of the Air & Waste Management Association* 55, 1158-1168, 2005.
- Dall'Osto, M., R. M. Harrison, H. Coe, P. I. Williams, and J. D. Allan, Real time chemical characterization of local and regional nitrate aerosols, *Atmos. Chem. Phys.*, 9, 3709-3720, 2009.
- Hering, S. and G. Cass, The Magnitude of Bias in the Measurement of Pm_{2.5} Arising from Volatilization of Particulate Nitrate from Teflon Filters, *Journal of the Air & Waste Management Association*, 49, 725-733, 1999.
- Mensah, A. A., R. Holzinger, R. Otjes, A. Trimborn, Th. F. Mentel, H. ten Brink, B. Hensing, and A. Kiendler-Scharr, Aerosol chemical composition at Cabauw, the Netherlands as observed in two intensive periods in May 2008 and March 2009, *Atmos. Chem. Phys.*, 12, 4723-4742, 2012.
- Morgan, W. T., J. D. Allan, K. N. Bower, M. Esselborn, B. Harris, J. S. Henzing, E. J. Highwood, A. Kiendler-Scharr, G. R. McMeeking, A. A. Mensah, M. J. Northway, S. Osborne, P. I. Williams, R. Krejci, and H. Coe, Enhancement of the aerosol direct radiative effect by semi-volatile aerosol components: airborne measurements in North-Western Europe, *Atmos. Chem. Phys.*, 10, 8151-8171, 2010.

221 Mozurkewich, M., The dissociation constant of ammonium nitrate and its dependence on
 222 temperature, relative humidity and particle size, *Atmos. Environ.*, 27A, 261-270, 1993.

223 Nenes, A., S. Pandis, and C. Pilinis, ISORROPIA: a new thermodynamic equilibrium model
 224 for multiphase multicomponent inorganic aerosols, *Aquat. Geochem.*, 4, 123-152, 1998.

225 Schaap, M., K. Muller and H. M. ten Brink, Constructing the European Aerosol Nitrate
 226 Concentration Field from Quality Analysed Data, *Atmospheric Environment*, 36, 1323-1335,
 227 2002.

228 Schaap, M., G. Spindler, M. Schulz, K. Acker, W. Maenhaut, A. Berner, W. Wieprecht, N.
 229 Streit, K. Muller, E. Brüggemann, X. Chi, J. P. Putaud, R. Hitzinger, H. Puxbaum, U.
 230 Baltensperger and H. ten Brink, Artefacts in the Sampling of Nitrate Studied in the Intercomp
 231 Campaigns of Eurotrac-Aerosol, *Atmospheric Environment*, 38, 6487-6496, 2004.

232 Schaap, M., R. P. Otjes, and E. P. Weijers, Illustrating the benefit of using hourly monitoring
 233 data on secondary inorganic aerosol and its precursors for model evaluation, *Atmos. Chem.*
 234 *Phys.*, 11, 11041-11053, 2011.

235 Seinfeld, J. H., and S. N. Pandis, *Atmospheric chemistry and Physics*, John Wiley and Sons,
 236 New York, 1998.

237 Sickles, J. E. and D. S. Shadwick, Biases in Clean Air Status and Trends Network Filter Pack
 238 Results Associated with Sampling Protocol, *Atmospheric Environment*, 36, 4687-4698, 2002.

239 Slanina, J., H. M. ten Brink, R. P. Otjes, A. Even, P. Jongejan, A. Khlystov, A. Waijers-
 240 Ijpelaan, M. Hu, and Y. Lu, The continuous analysis of nitrate and ammonium in aerosols by
 241 the steam jet aerosol collector (SJAC): extension and validation of the methodology, *Atmos.*
 242 *Environ.*, 35, 2319-2330, 2001.

243 Ten Brink, H., R. Otjes, P. Jongejan, S. Slanina, An instrument for semi-continuous
 244 monitoring of the size-distribution of nitrate, ammonium, sulphate and chloride in aerosol,
 245 *Atmos. Environ.*, 41, 2768-2779, 2007.

246 Trebs, I., F. X. Meixner, J. Slanina, R. Otjes, P. Jongejan, and M. O. Andreae, Real-time
 247 measurements of ammonia, acidic trace gases and water-soluble inorganic aerosol species at a
 248 rural site in the Amazon Basin, *Atmos. Chem. Phys.*, 4, 967-987, 2004.

249 Vecchi, R., G. Valli, P. Fermo, A. D'Alessandro, A. Piazzalunga and V. Bernardoni, Organic
250 and Inorganic Sampling Artefacts Assessment, *Atmospheric Environment*, 43, 1713-1720,
251 2009.

252 Yu, X. Y., L. Tachyoung, B. Ayres, S. M. Kreidenweis, J. L. Collett and W. Maim.
253 Particulate Nitrate Measurement Using Nylon Filters, *Journal of the Air & Waste*
254 *Management Association*, 55, 1100-1110, 2005.

255

Figure Captions

Figure S1. Variation of NO_3^- (blue) and NH_4^+ (red) equilibrium concentrations ($\mu\text{g}/\text{m}^3$) as a function of total sulfate, total ammonia, total nitrate ($\mu\text{g}/\text{m}^3$), relative humidity (%) and temperature (T). INCA model results : solid line, ISORROPIA model: triangles.

Figure S2. Simulated diurnal variation of NO_3^- surface concentration ($\mu\text{g}/\text{m}^3$) during the 1/08/2009 to 30/10/2009 period in England, the Po valley, The Netherlands, and in Northern China.

Figure S3. Annual mean tropospheric column of (top) fine mode nitrate aerosols, (middle) coarse mode nitrates on dust, and (bottom) coarse mode nitrates on sea-salt simulated for present-day conditions (mg/m^2).

Figure S4. Simulated surface concentration of sulfates ($\mu\text{S}/\text{m}^3$), ammonium ($\mu\text{N}/\text{m}^3$), and nitrates ($\mu\text{N}/\text{m}^3$) for the year 2006 compared to EBAS data over the world (all available data). Dashed lines indicate 1:2 and 2:1 ratios.

Figure S5. Simulated surface concentration of sulfates ($\mu\text{S}/\text{m}^3$), ammonium ($\mu\text{N}/\text{m}^3$), and nitrates ($\mu\text{N}/\text{m}^3$) for the year 2006 compared to EBAS data over Europe. Dashed lines indicate 1:2 and 2:1 ratios.

Figure S6. Simulated surface concentration of sulfates ($\mu\text{S}/\text{m}^3$), ammonium ($\mu\text{N}/\text{m}^3$), and nitrates ($\mu\text{N}/\text{m}^3$) for the year 2006 compared to EBAS data over Northern America. Dashed lines indicate 1:2 and 2:1 ratios.

Figure S7. Simulated SO_x ($\text{gS/m}^2/\text{yr}$), NH_x and NO_y ($\text{gN/m}^2/\text{yr}$) wet deposition for the year 2006 compared to EBAS data for the world (all available data). Dashed lines indicate 1:2 and 2:1 ratios.

Figure S8. Simulated SO_x ($\text{gS/m}^2/\text{yr}$), NH_x and NO_y ($\text{gN/m}^2/\text{yr}$) wet deposition for the year 2006 compared to EBAS data over Europe. Dashed lines indicate 1:2 and 2:1 ratios.

Figure S9. Simulated SO_x ($\text{gS/m}^2/\text{yr}$), NH_x and NO_y ($\text{gN/m}^2/\text{yr}$) wet deposition for the year 2006 compared to EBAS data over Northern America. Dashed lines indicate 1:2 and 2:1 ratios.

Figure S10. Simulated SO_x ($\text{gS/m}^2/\text{yr}$), NH_x and NO_y ($\text{gN/m}^2/\text{yr}$) wet deposition for the year 2006 compared to EBAS data over Eastern Asia. Dashed lines indicate 1:2 and 2:1 ratios.

Figure S11. Simulated total aerosol optical depth at 550 nm for the year 2006 compared to the AERONET data worldwide (all available data), over Europe, Northern America, Northern Africa, and Eastern Asia. Dashed lines indicate 1:2 and 2:1 ratios.

Figure S12. Changes in ammonia surface concentration ($\mu\text{g/m}^3$) relative to the present-day distribution for scenario RCP8.5 (top) and RCP4.5 (bottom) calculated for 2030 (left) and 2100 (right).

Figure S13. Changes in nitric acid surface concentration ($\mu\text{g/m}^3$) relative to the present-day distribution for scenario RCP8.5 (top) and RCP4.5 (bottom) calculated for 2030 (left) and 2100 (right).

Figure S14. Changes in sulfate surface concentration ($\mu\text{g}/\text{m}^3$) relative to the present-day distribution for scenario RCP8.5 (top) and RCP4.5 (bottom) calculated for 2030 (left) and 2100 (right).

Figure S15. Changes in nitrate surface concentration ($\mu\text{g}/\text{m}^3$) relative to the present-day distribution for scenario RCP8.5 (top) and RCP4.5 (bottom) calculated for 2030 (left) and 2100 (right).

Figure S16. Changes in nitrate column (mg/m^2) relative to the present-day distribution for scenario RCP8.5 (top) and RCP4.5 (bottom) calculated for 2030 (left) and 2100 (right).

Figure S17. Evolution of $\text{NH}_x + \text{NO}_y$ total deposition ($\text{mgN}/\text{m}^2/\text{yr}$) for scenario RCP8.5 (red), RCP6.0 (yellow), RCP4.5 (green) and RCP2.6 (blue) between present-day and 2100. The averaged deposition is depicted for Europe, Northern America, Northern Asia, Southern Asia, India, Africa, Southern America, Australia, the global ocean, and the globe.

Figure S18. Evolution of the NH_x fractional contribution to $\text{NH}_x + \text{NO}_y$ total deposition (%) for scenario RCP8.5 (red), RCP6.0 (yellow), RCP4.5 (green) and RCP2.6 (blue) between present-day and 2100. The averaged deposition is depicted for Europe, Northern America, Northern Asia, Southern Asia, India, Africa, Southern America, Australia, the global ocean, and the globe.

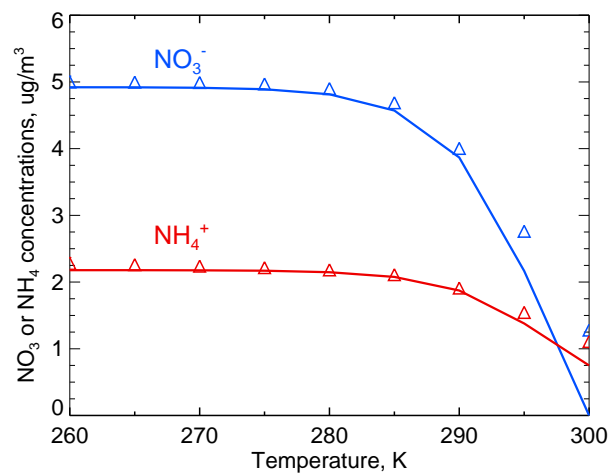
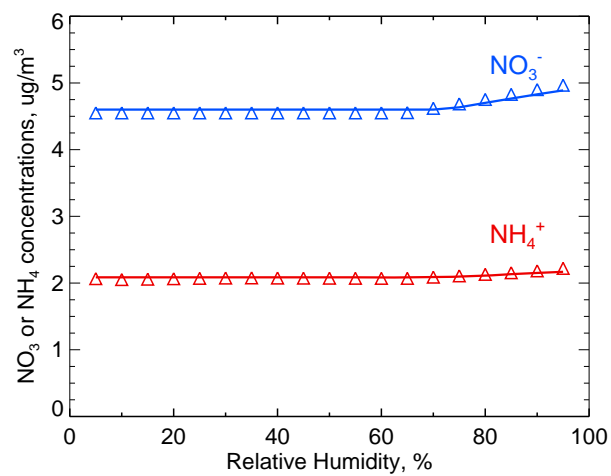
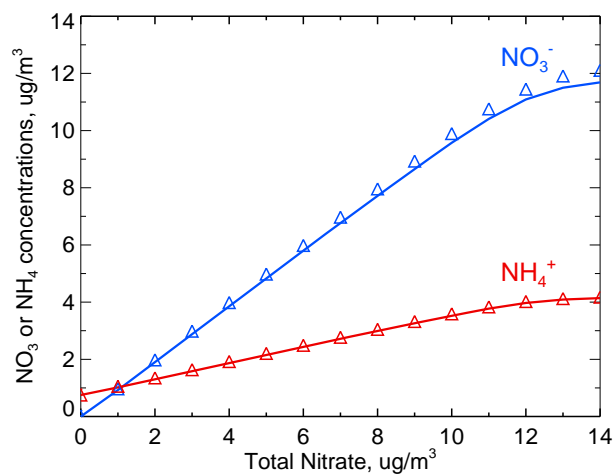
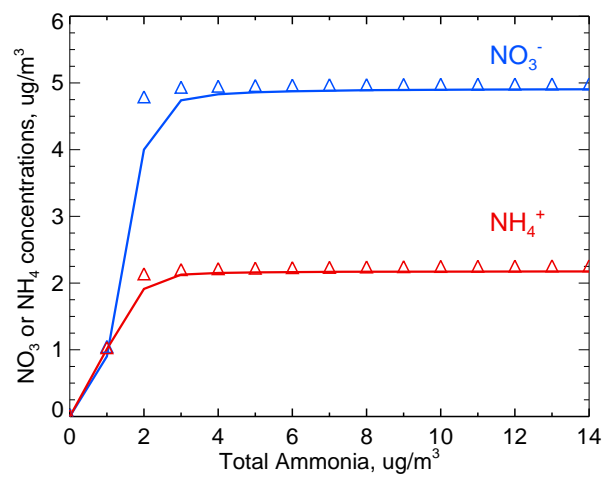
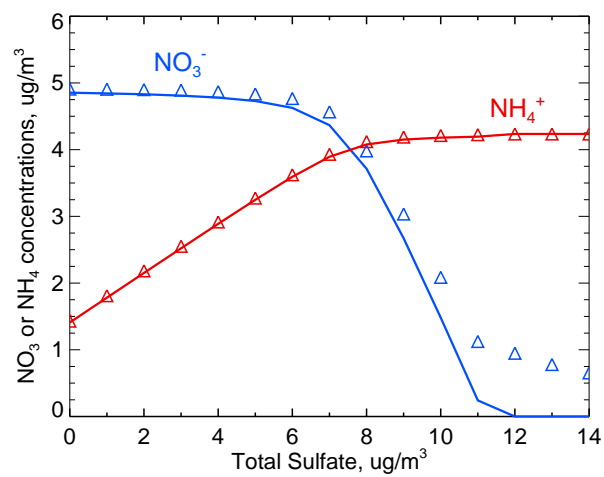


Figure S1

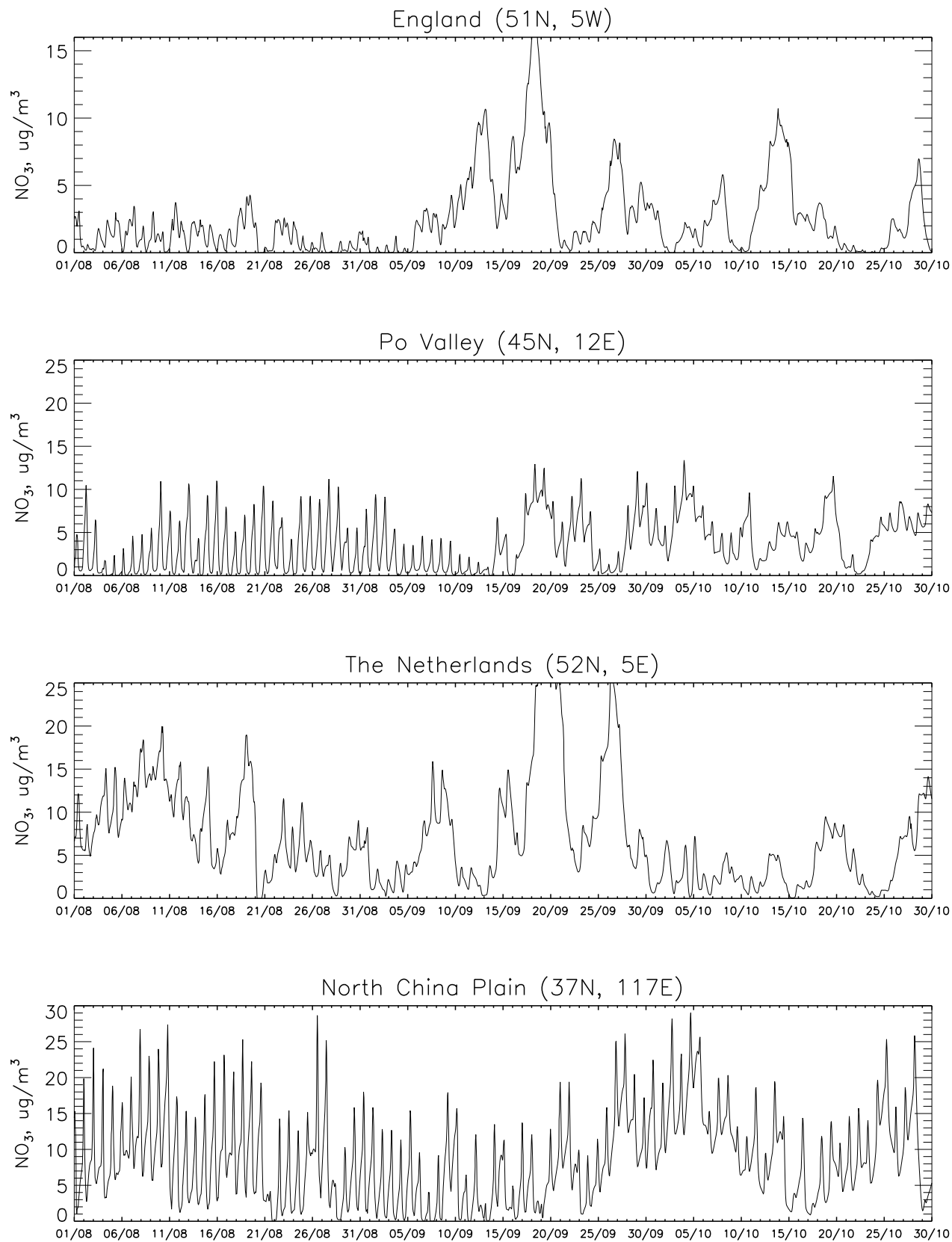


Figure S2

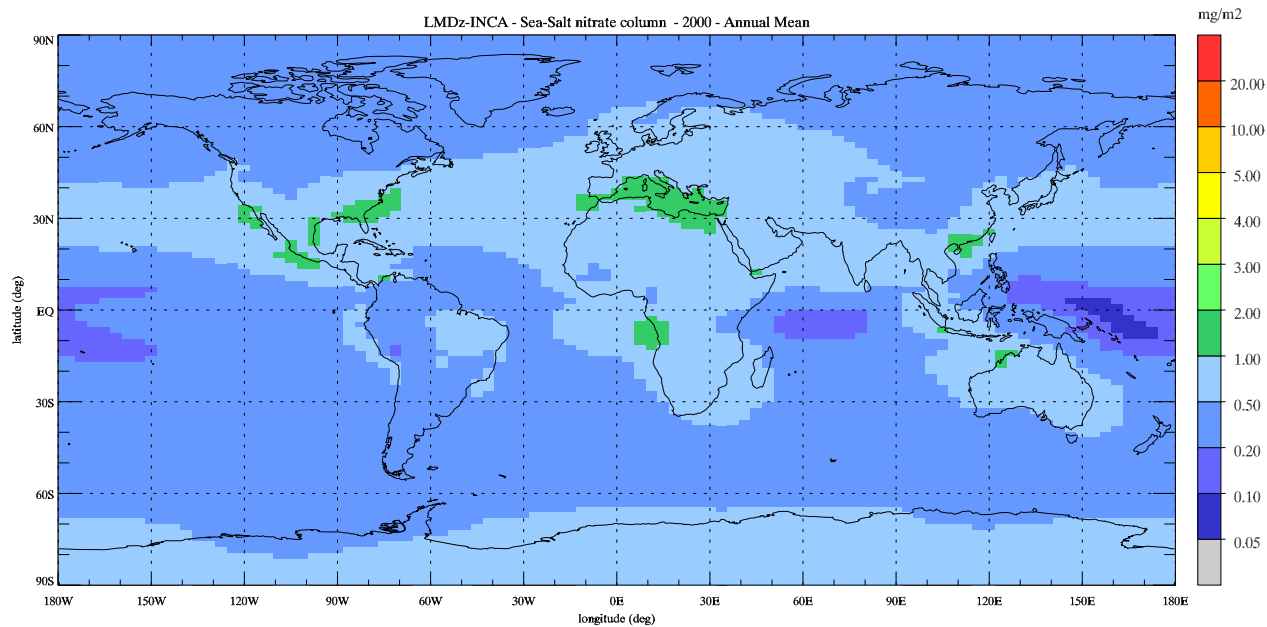
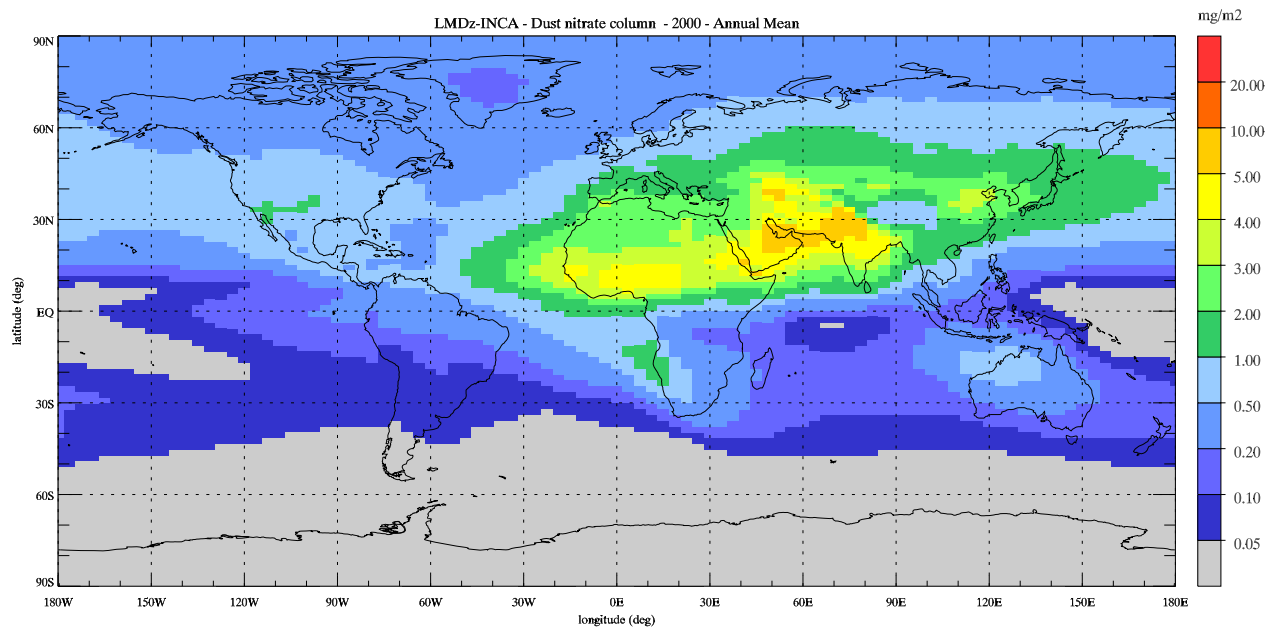
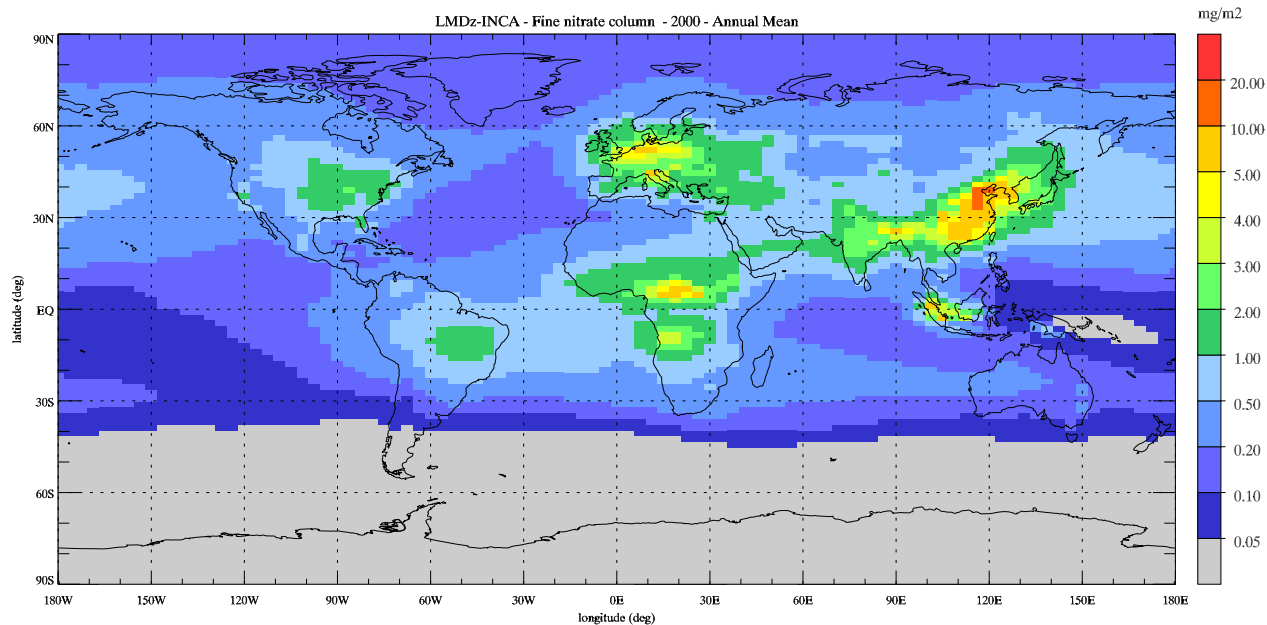


Figure S3

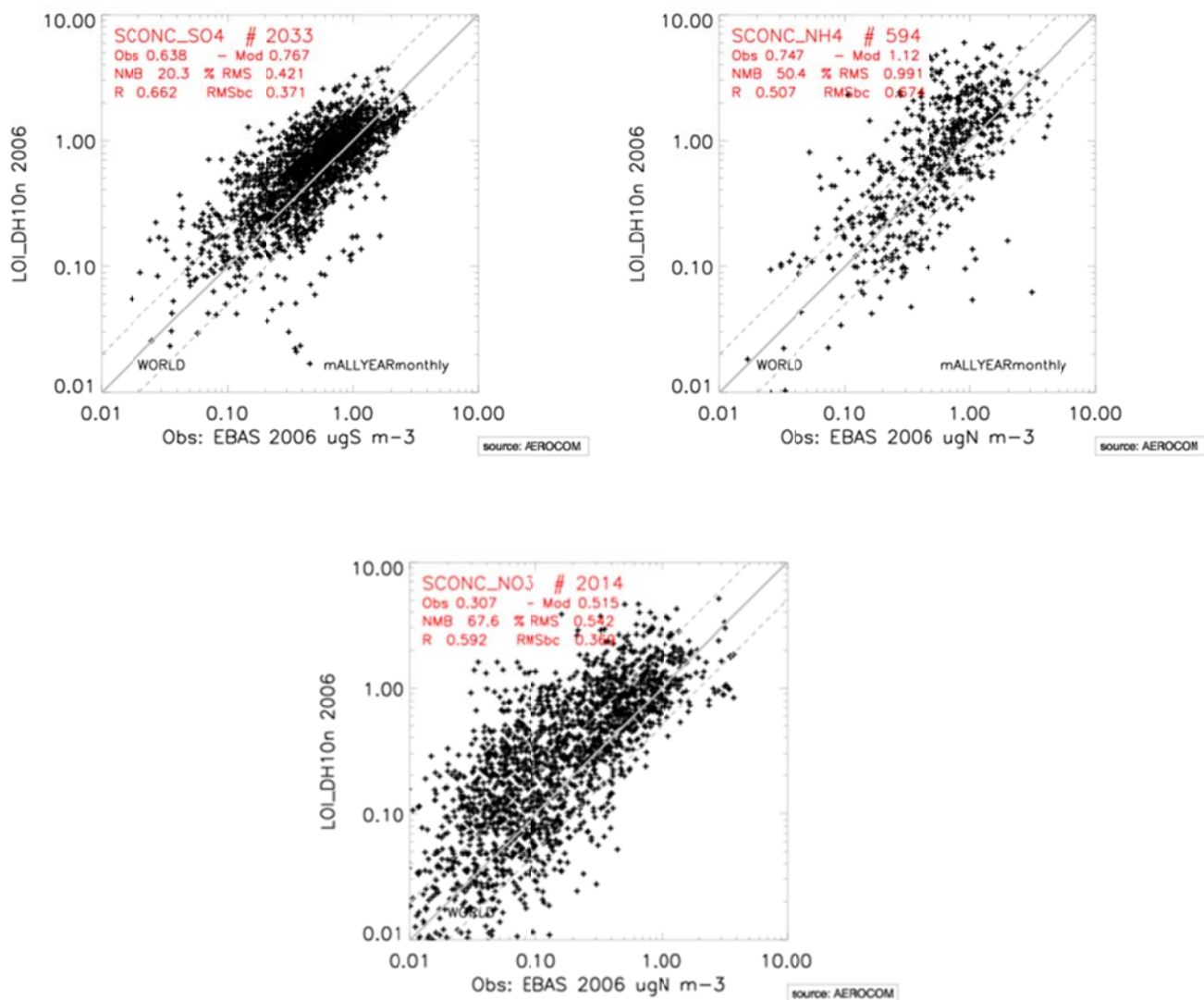


Figure S4

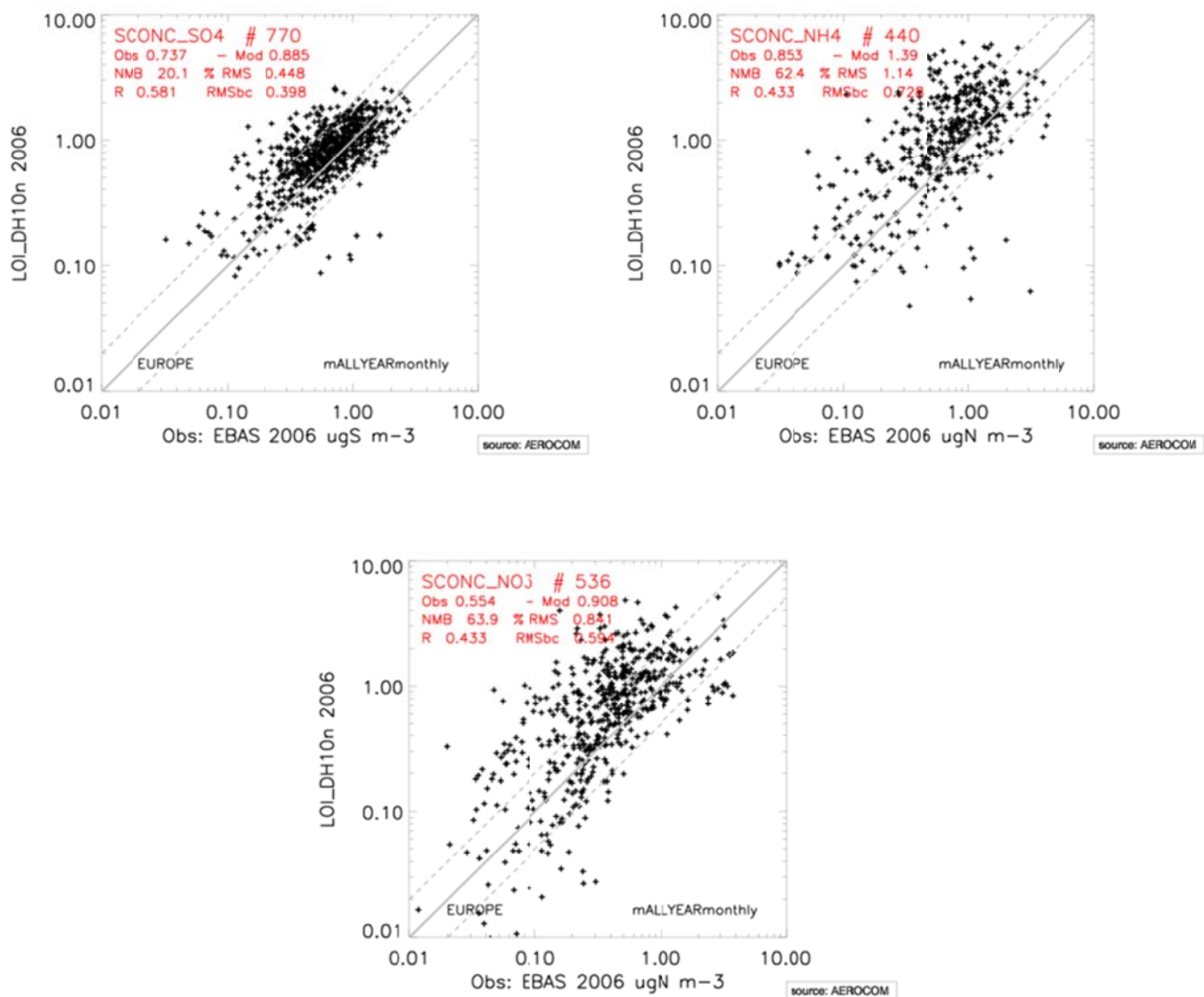


Figure S5

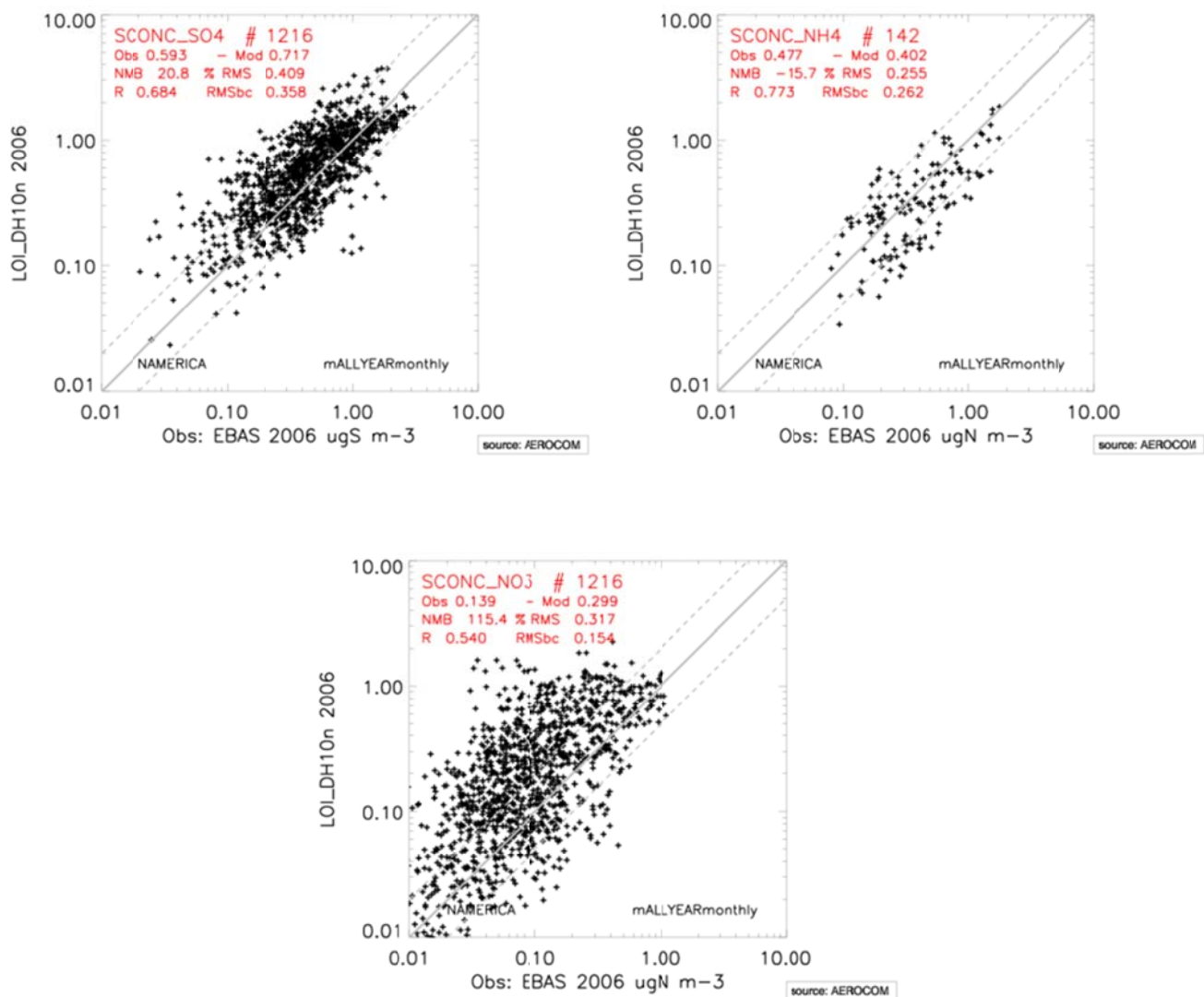


Figure S6

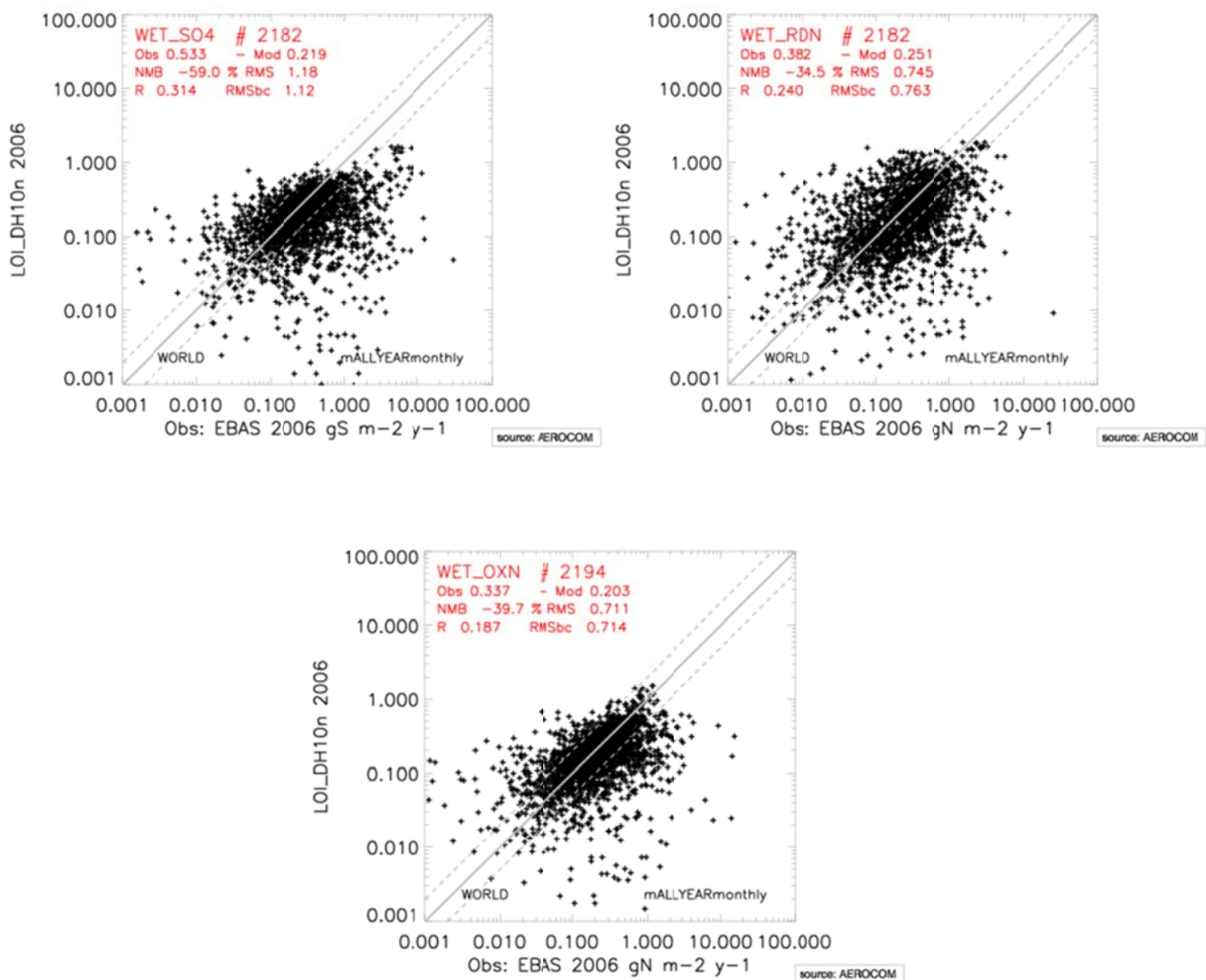
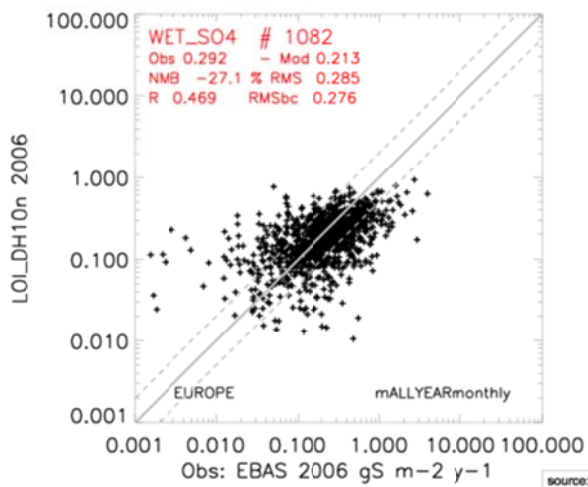
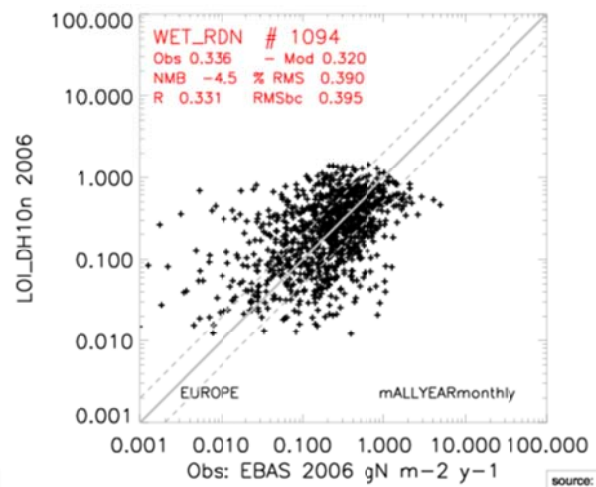


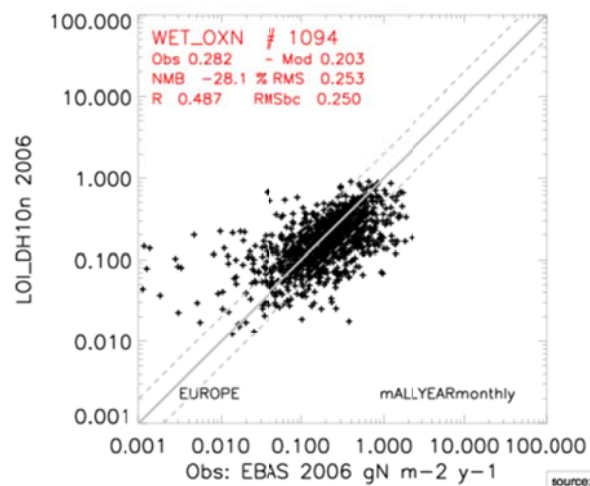
Figure S7



source: AEROCOM

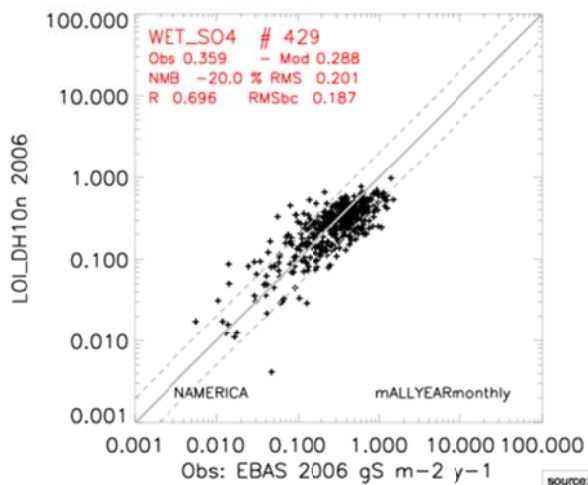


source: AEROCOM

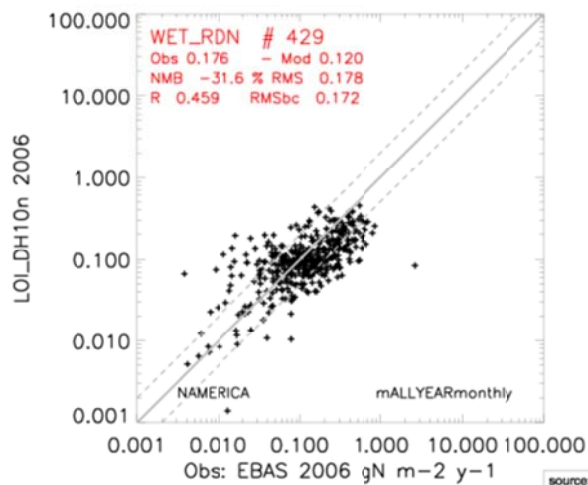


source: AEROCOM

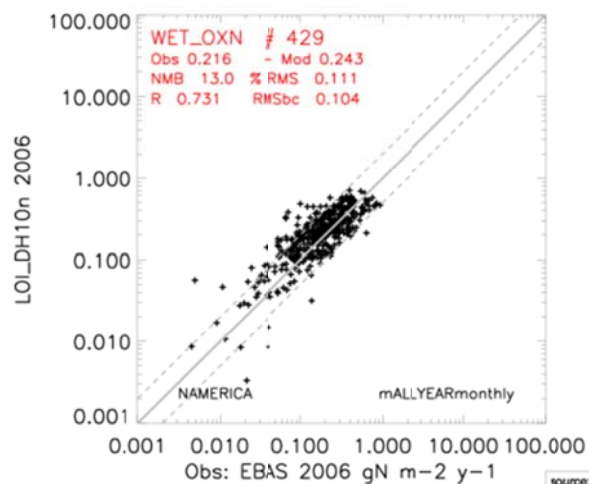
Figure S8



source: AEROCOM



source: AEROCOM



source: AEROCOM

Figure S9

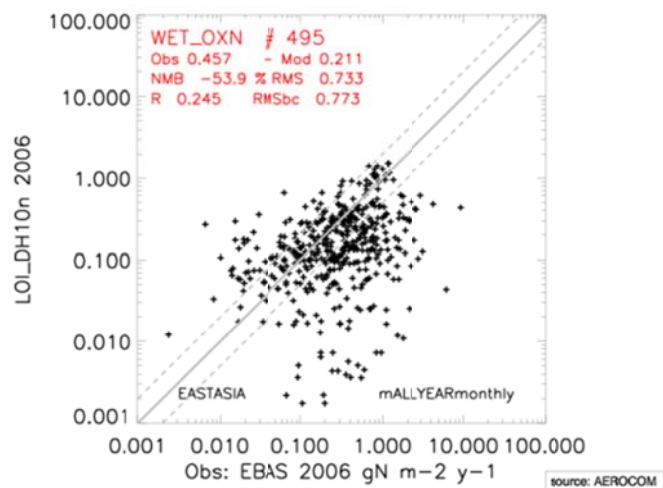
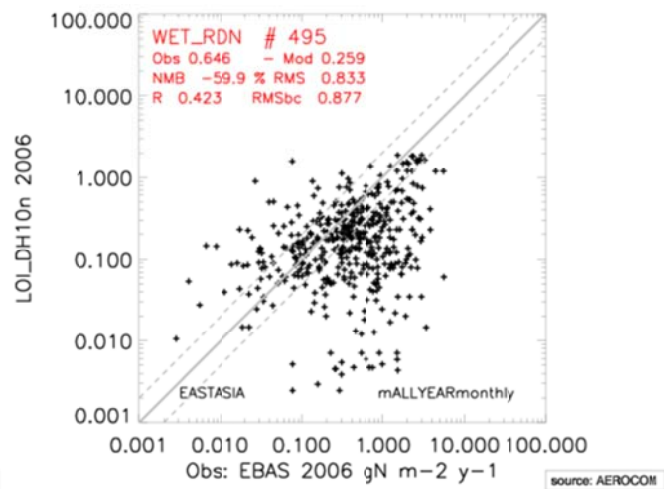
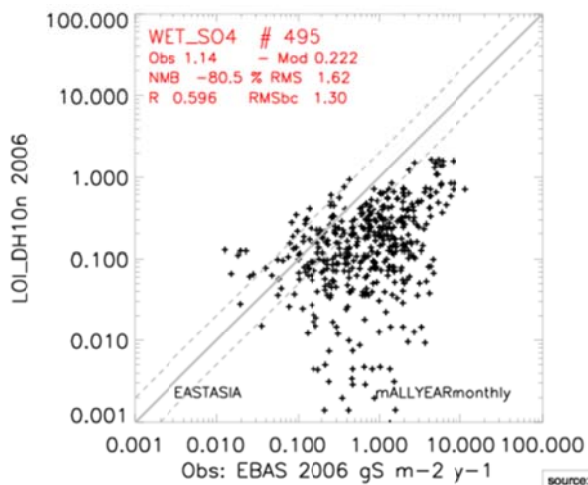


Figure S10

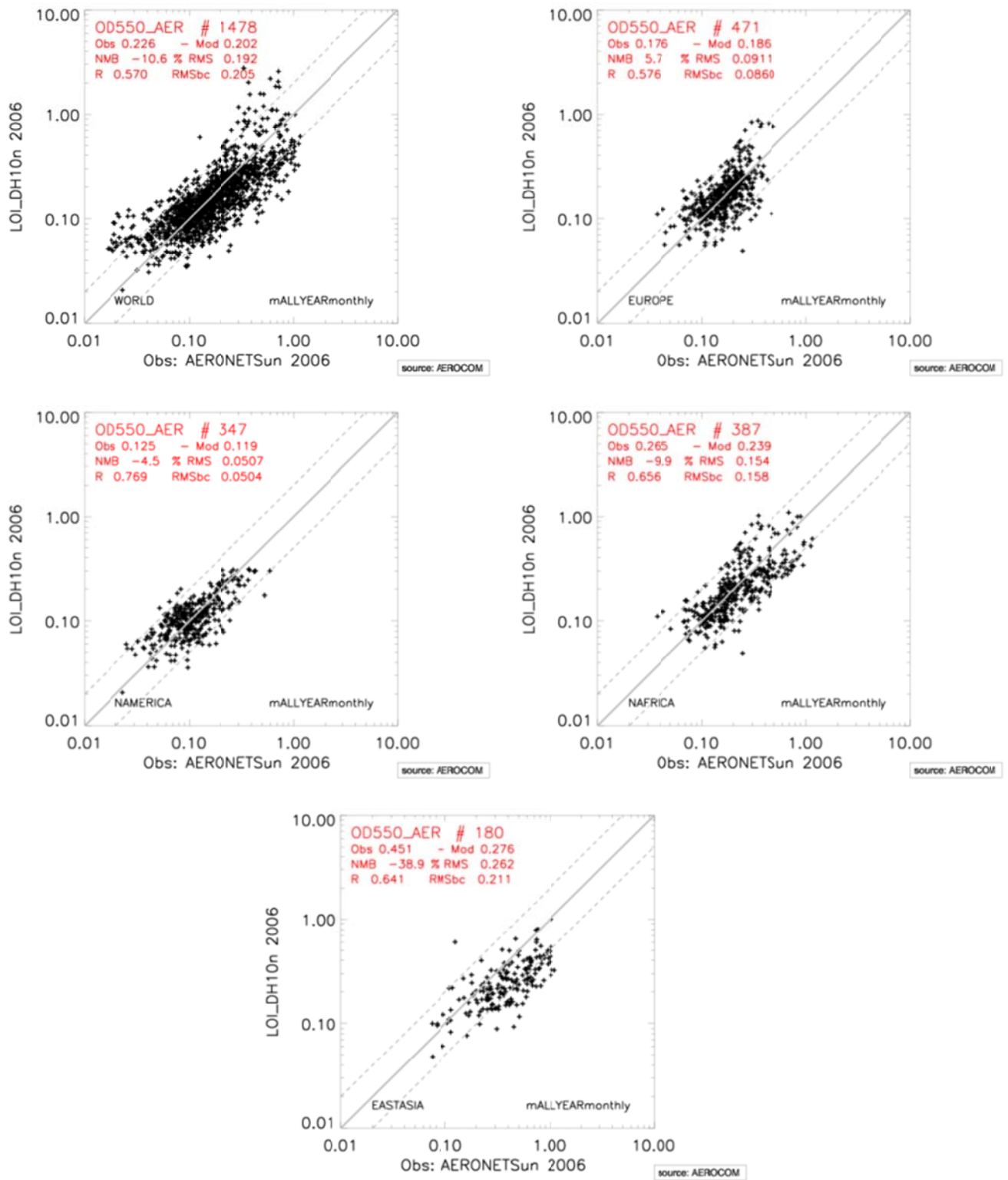


Figure S11

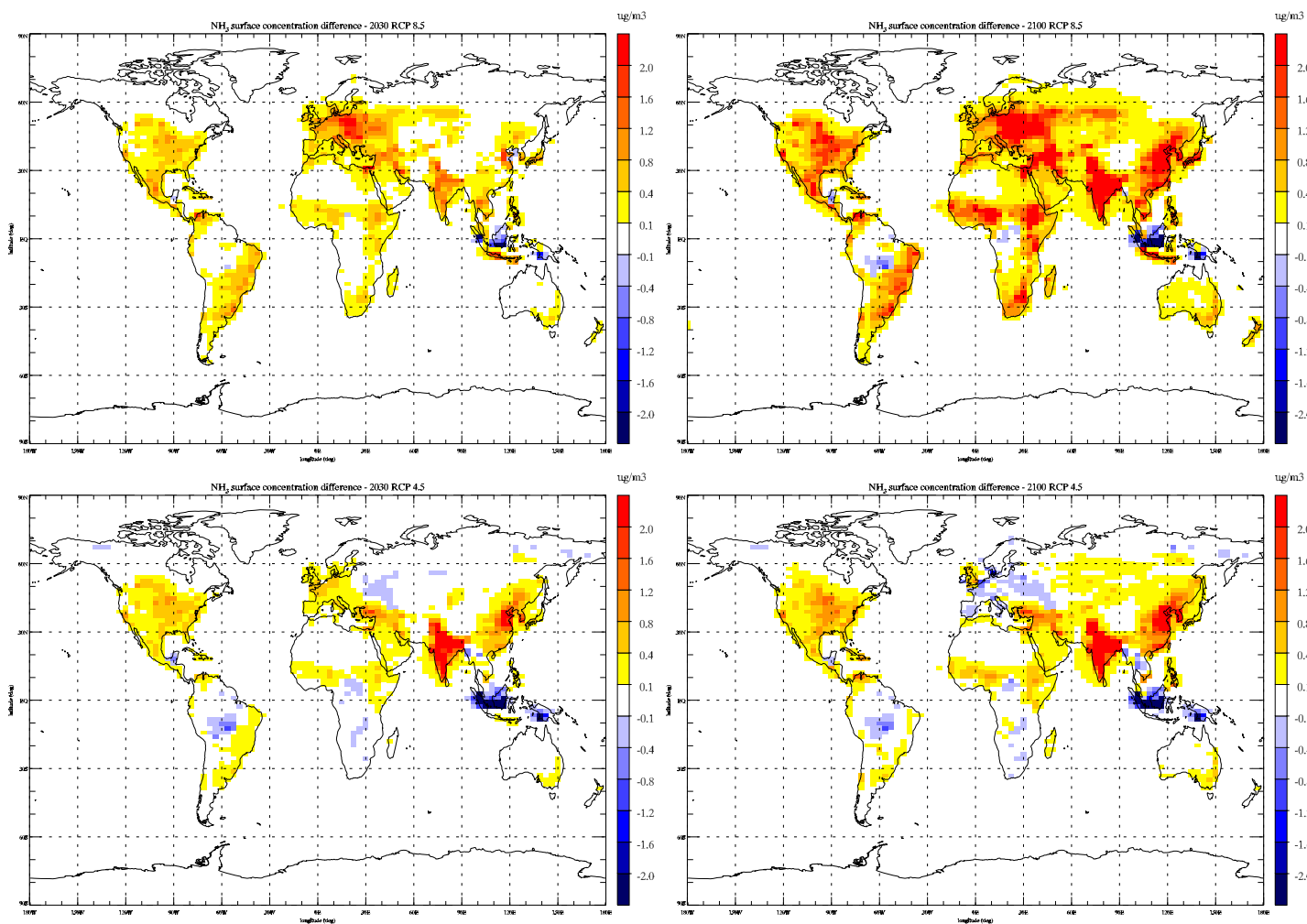


Figure S12

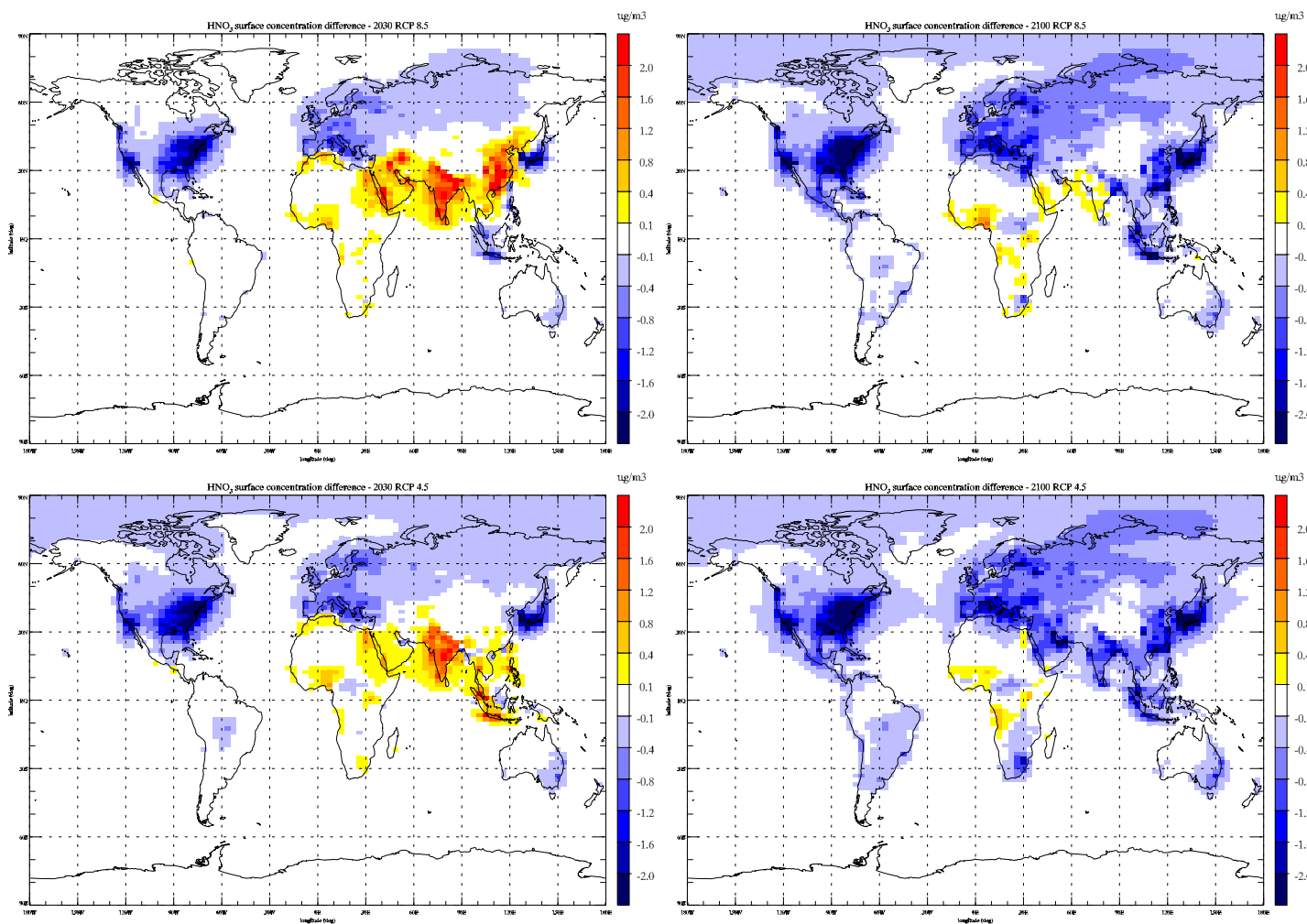


Figure S13

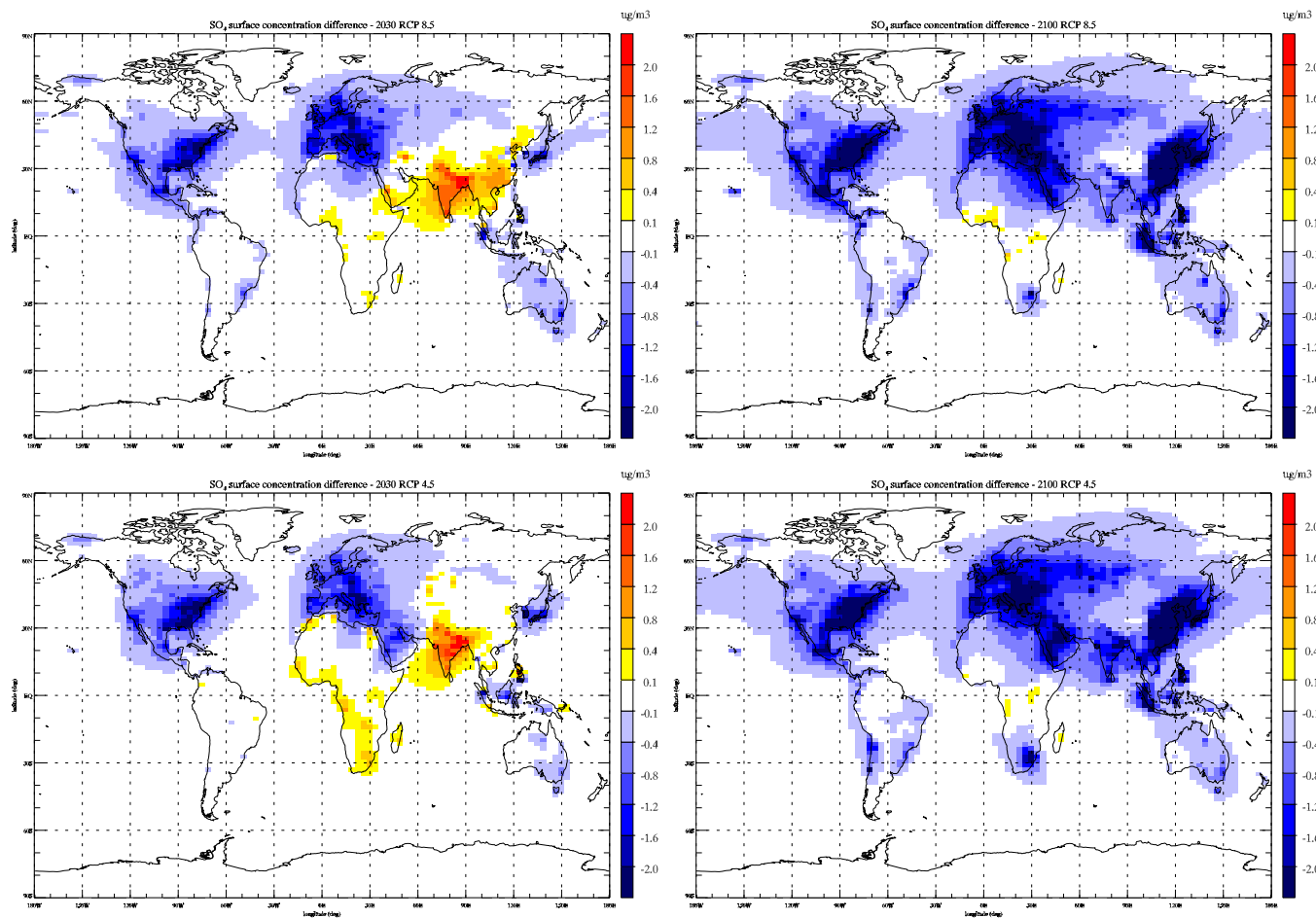


Figure S14

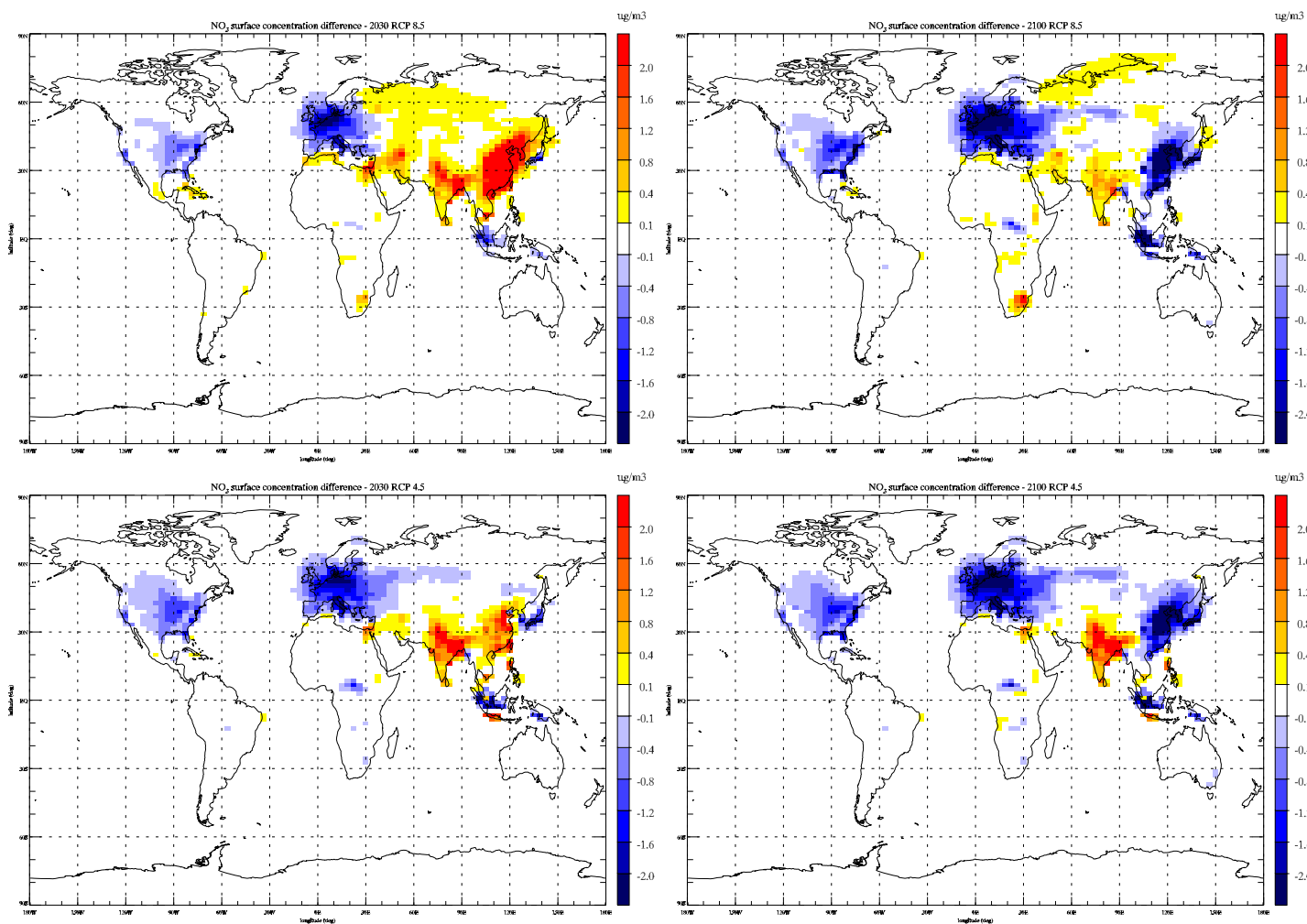


Figure S15

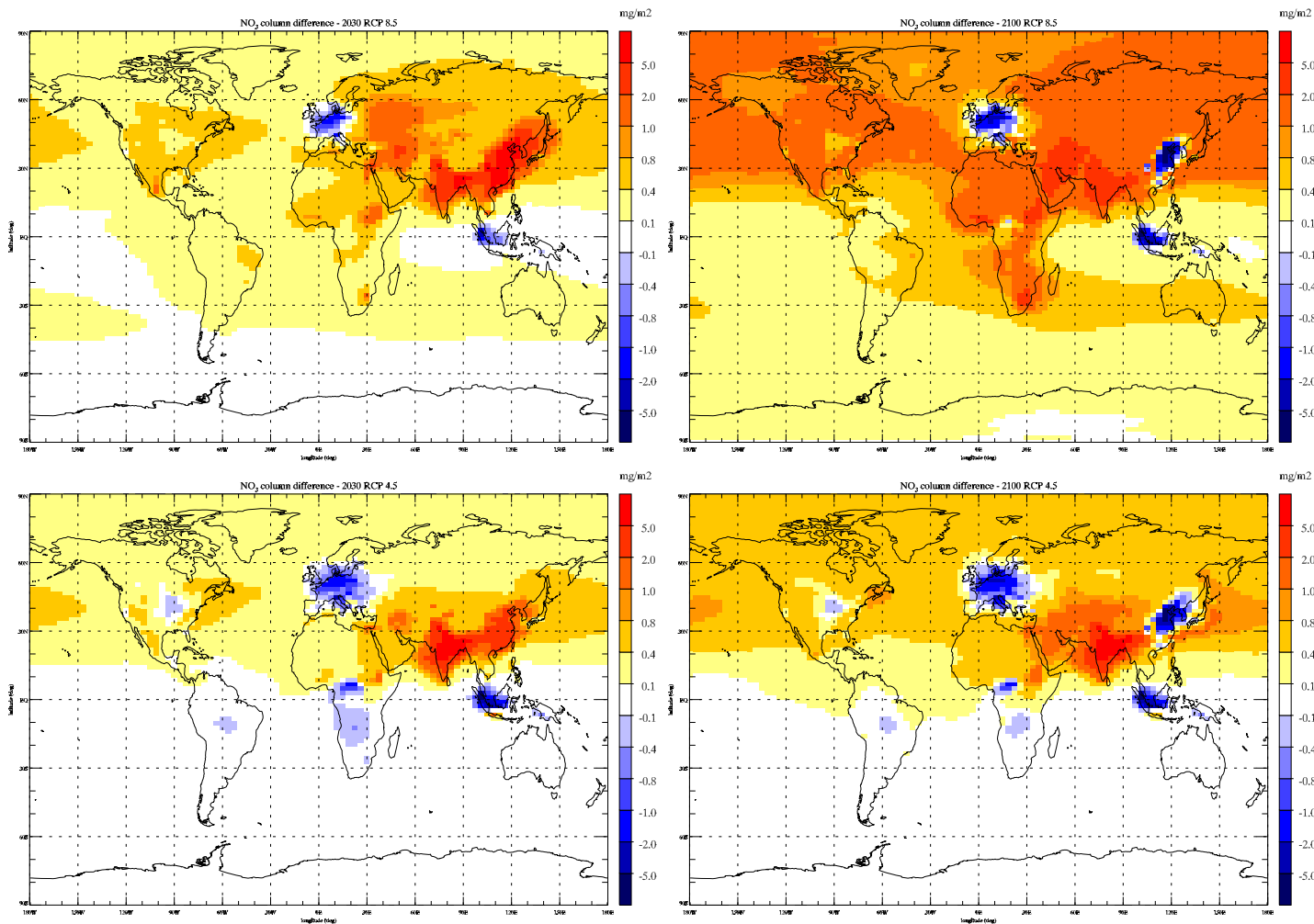


Figure S16

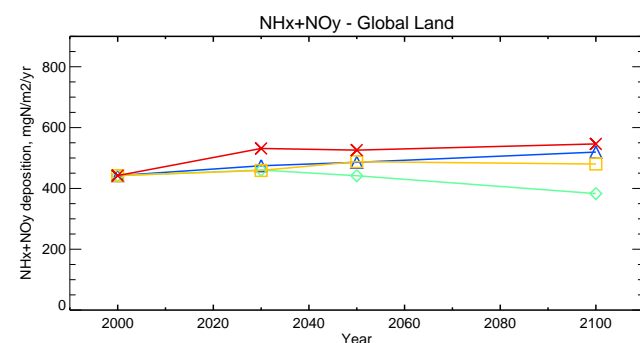
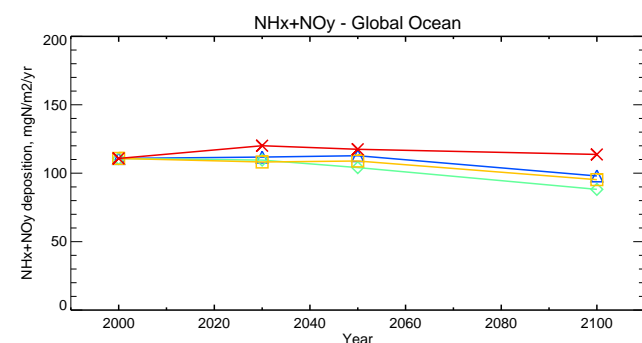
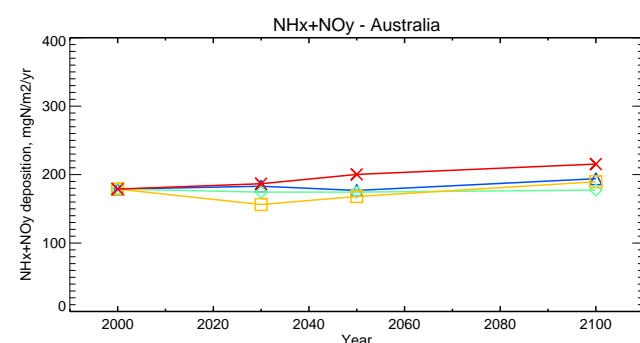
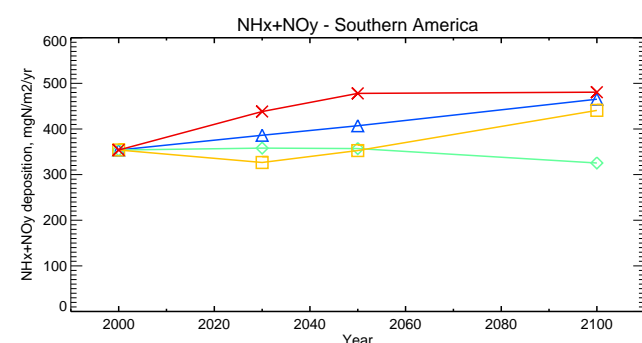
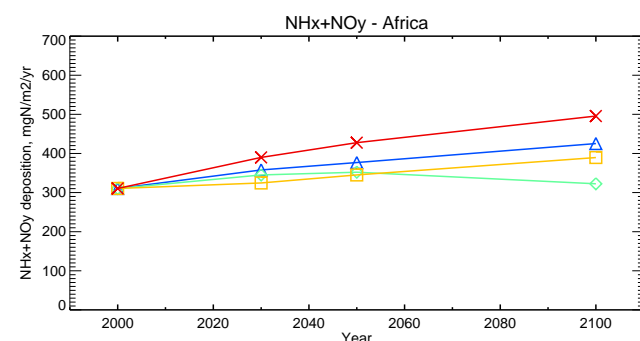
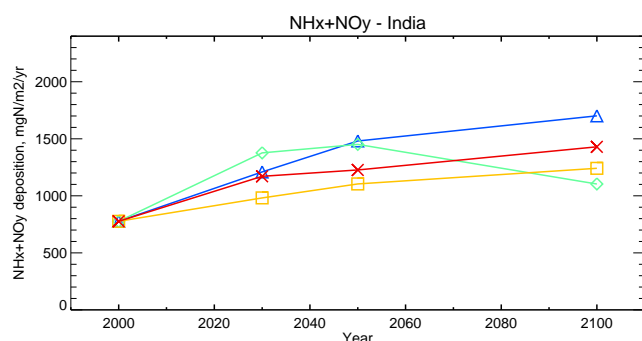
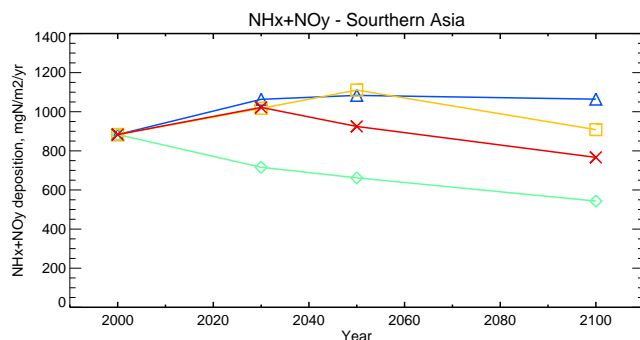
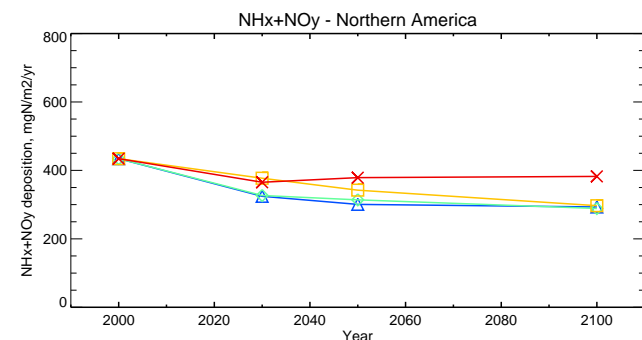
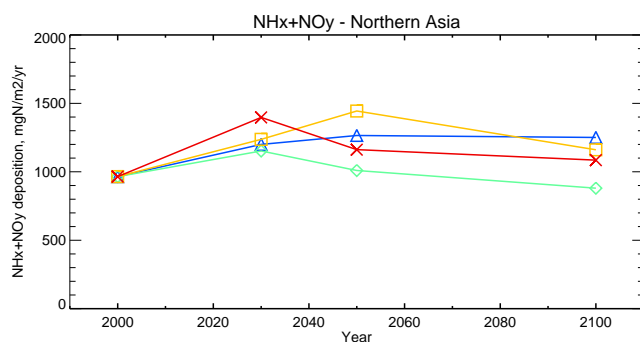
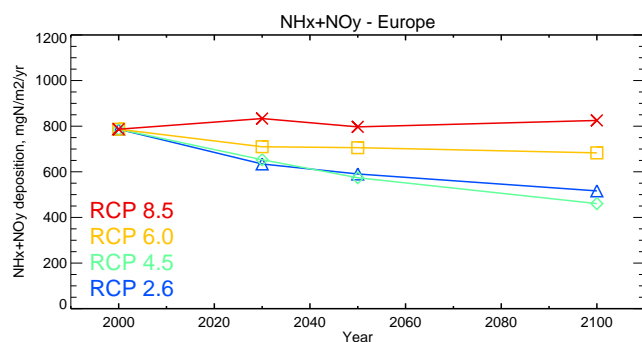


Figure S17

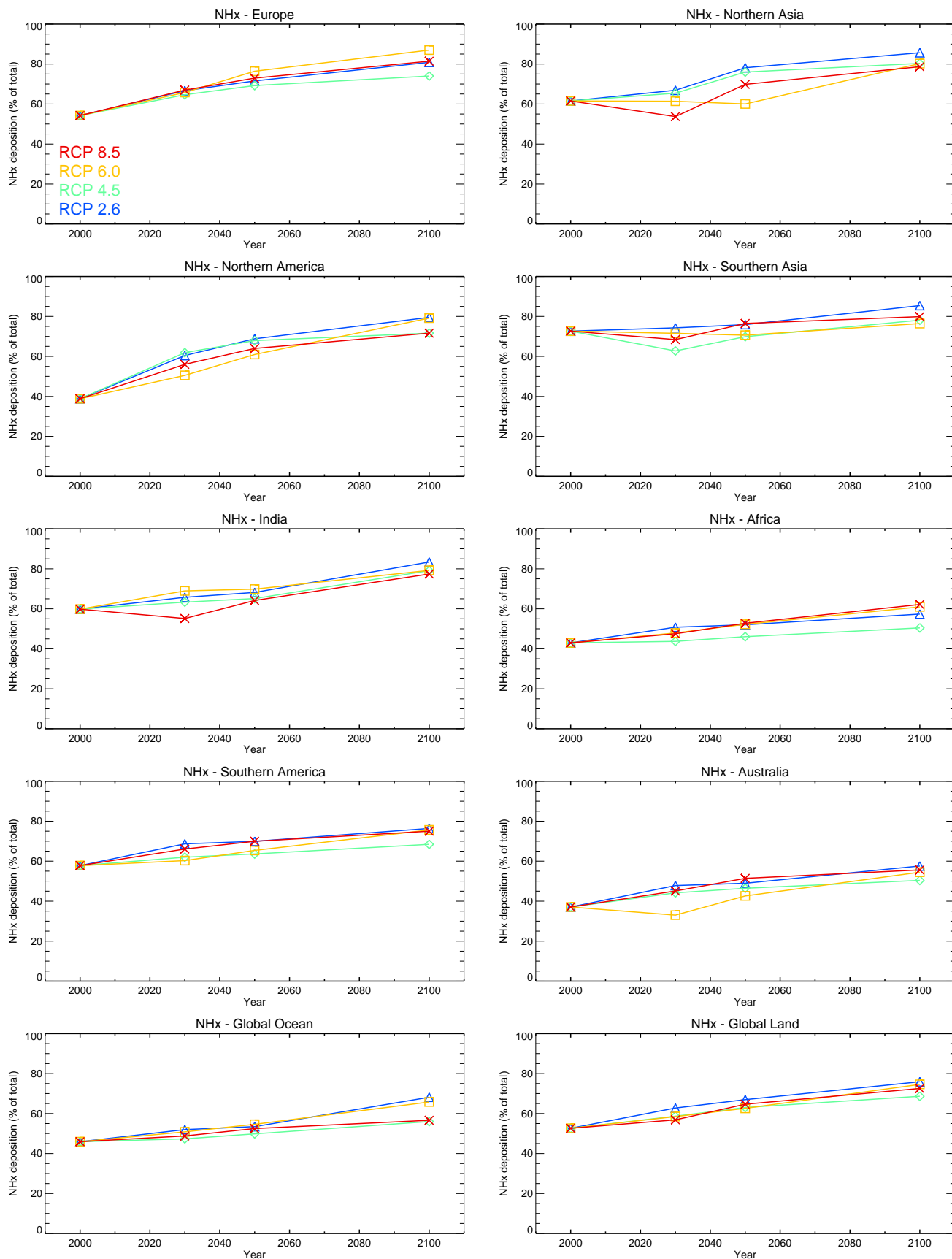


Figure S18